Identification of the simplest sugar-like molecule glycolaldehyde towards the hot molecular core G358.93–0.03 MM1

Arijit Manna [1], Sabyasachi Pal [1]★ Serena Viti[2,3] and Sekhar Sinha[1]

[1]*Department of Physics and Astronomy, Midnapore City College, Paschim Medinipur, West Bengal 721129, India*
[2]*Leiden Observatory, Leiden University, P.O. Box 9513, NL-2300 RA Leiden, the Netherlands*
[3]*Department of Physics and Astronomy, UCL, Gower Street, London WC1E 6BT, UK*

ABSTRACT

Glycolaldehyde (CH_2OHCHO) is the simplest monosaccharide sugar in the interstellar medium, and it is directly involved in the origin of life via the 'RNA world' hypothesis. We present the first detection of CH_2OHCHO towards the hot molecular core G358.93–0.03 MM1 using the Atacama Large Millimetre/Submillimetre Array (ALMA). The calculated column density of CH_2OHCHO towards G358.93–0.03 MM1 is $(1.52 \pm 0.9) \times 10^{16}$ cm^{-2} with an excitation temperature of 300 ± 68.5 K. The derived fractional abundance of CH_2OHCHO with respect to H_2 is $(4.90 \pm 2.92) \times 10^{-9}$, which is consistent with that estimated by existing two-phase warm-up chemical models. We discuss the possible formation pathways of CH_2OHCHO within the context of hot molecular cores and hot corinos and find that CH_2OHCHO is likely formed via the reactions of radical HCO and radical CH_2OH on the grain-surface of G358.93–0.03 MM1.

Key words: astrochemistry – stars: formation – ISM: abundances – ISM: individual objects (G358.93–0.03 MM1) – ISM: kinematics and dynamics.

1 INTRODUCTION

In the interstellar medium (ISM), glycolaldehyde (CH_2OHCHO) is known as one of the simplest aldehyde sugar, and it is the only sugar detected in space (Hollis et al. 2004). The monosaccharide sugar molecule CH_2OHCHO is an isomer of both methyl formate (CH_3OCHO) and acetic acid (CH_3COOH; Beltrán et al. 2009; Mininni et al. 2020). CH_2OHCHO is one of the important interstellar organic molecule in the ISM because when CH_2OHCHO reacts with propenal (CH_2CHCHO), it forms ribose ($C_5H_{10}O_5$) (Beltrán et al. 2009). Ribose ($C_5H_{10}O_5$) is known as the central constituent of RNA, and it is directly involved in the hypothesis of the origin of life in the universe. The organic molecule CH_2OHCHO also has a major role in the formation of three, four, and five-carbon sugars (Halfen et al. 2006). The molecular lines of CH_2OHCHO were first detected towards Sgr B2 (N; Hollis, Lovas & Jewell 2000; Hollis et al. 2001, 2004; Halfen et al. 2006; Belloche et al. 2013; Xue et al. 2019) and subsequently towards the hot molecular core G31.41+0.31 (Beltrán et al. 2009; Calcutt et al. 2014; Rivilla et al. 2017; Mininni et al. 2020), the solar-like protostar IRAS 16293–2422 B (Jørgensen et al. 2012; Rivilla et al. 2019), the class 0 protostar NGC 7129 FIRS 2 (Fuente et al. 2014), and the hot corino NGC 1333 IRAS2A (Coutens et al. 2015). Recently, emission lines of CH_2OHCHO were also tentatively detected from the hot molecular core G10.47 + 0.03 (Mondal et al. 2021).

The chemistry of hot cores is characterized by the sublimation of ice mantles, which accumulate during the star-formation process (Shimonishi et al. 2021). In prestellar cores and cold molecular clouds, the atoms and gaseous molecules freeze on to the dust grains. During the process of star-formation, the thermal energy and pressure increase due to the gravitational collapse. Therefore, dust temperatures also increase, and chemical interactions between heavy species become active on the grain-surfaces (Garrod & Herbst 2006; Shimonishi et al. 2021). This leads to the formation of large complex organic molecules (Garrod & Herbst 2006; Shimonishi et al. 2021). In addition, sublimated molecules such as ammonia (NH_3) and methanol (CH_3OH) are also subject to further gas-phase reactions (Nomura & Miller 2004; Taquet, Wirström & Charnley 2016; Shimonishi et al. 2021). Consequently, the warm and dense gas surrounding the protostars becomes chemically rich, resulting in the formation of one of the strongest and most powerful molecular line emitters known as hot molecular cores (Shimonishi et al. 2021). Hot molecular cores are ideal targets for astrochemical studies because a variety of simple and complex organic molecules are frequently found towards these objects (Herbst & van Dishoeck 2009). They are one of the earliest stages of star-formation and play an important role in increasing the chemical complexity of the ISM (Shimonishi et al. 2021). Hot molecular cores are small, compact objects ($\leq$0.1 pc) with a warm temperature ($\geq$100 K) and high-gas density ($n_{H_2} \geq 10^6$ cm^{-3}) that promote molecular evolution by thermal hopping on dust grains (van Dishoeck & Blake 1998; Williams & Viti 2014). The lifetime of hot molecular cores is thought to be approximately 10^5 years (medium warm-up phase) to 10^6 years (slow warm-up phase; van Dishoeck & Blake 1998; Viti et al. 2004; Garrod & Herbst 2006; Garrod, Widicus Weaver & Herbst 2008; Garrod 2013).

The hot molecular core candidate G358.93–0.03 MM1 is located in the high-mass star-formation region G358.93–0.03 at a

★ E-mail: sabya.pal@gmail.com

distance of 6.75 $^{+0.37}_{-0.68}$ kpc (Reid et al. 2014; Brogan et al. 2019). The total gas mass of G358.93–0.03 is 167 $\pm$ 12M$_\odot$ and its luminosity is $\sim$7.7 $\times$ 10^{3}L$_\odot$ (Brogan et al. 2019). The high-mass star-formation region G358.93–0.03 contains eight submillimetre continuum sources, which are designated as G358.93–0.03 MM1 to G358.93–0.03 MM8 in order of decreasing right ascension (Brogan et al. 2019). G358.93–0.03 MM1 is the brightest sub-millimetre continuum source that hosts a line-rich hot molecular core (Brogan et al. 2019; Bayandina et al. 2022). Previously, maser lines of deuterated water (HDO), isocyanic acid (HNCO), and methanol (CH$_3$OH) were detected towards G358.93–0.03 MM1 using the Atacama Large Millimetre/Submillimetre Array (ALMA), Tianma Radio Telescope (TMRT), and Very Large Array (VLA) radio telescopes (Brogan et al. 2019; Chen et al. 2020). The rotational emission lines of methyl cyanide (CH$_3$CN) with transition J = 11(4)–10(4) were also detected from both G358.93–0.03 MM1 and G358.93–0.03 MM3 using the ALMA (Brogan et al. 2019). The excitation temperature of CH$_3$CN towards the G358.93–0.03 MM1 and G358.93–0.03 MM3 is 172 $\pm$ 3 K (Brogan et al. 2019). The systematic velocities of G358.93–0.03 MM1 and G358.93–0.03 MM3 are –16.5 $\pm$ 0.3 and –18.6 $\pm$ 0.2 km s^{-1}, respectively (Brogan et al. 2019). Recently, rotational emission lines of the possible urea precursor molecule cyanamide (NH$_2$CN) were also detected towards G358.93–0.03 MM1 using the ALMA (Manna & Pal 2023).

In this article, we present the first detection of the simplest sugar-like molecule CH$_2$OHCHO towards the hot molecular core G358.93–0.03 MM1 using the ALMA. ALMA data and their reductions are presented in Section 2. The line identification and the determination of the physical properties of the gas are presented in Section 3. A discussion on the origin of CH$_2$OHCHO in this hot molecular core and conclusions are shown in Sections 4 and 5, respectively.

2 OBSERVATIONS AND DATA REDUCTION

The high-mass star-forming region G358.93–0.03 was observed using the ALMA band 7 receivers (PI: Crystal Brogan). The observation of G358.93–0.03 was performed on 2019 October 11, with a phase centre of (α, δ)$_{J2000}$ = (17:43:10.000, −29:51:46.000) and an on-source integration time of 756.0 s. During the observations, a total of 47 antennas were used, with a minimum baseline of 14 m and a maximum baseline of 2517 m. J1550+0527 was used as the flux calibrator and bandpass calibrator, and J1744–3116 was used as the phase calibrator. The observed frequency ranges of G358.93–0.03 were 290.51–292.39, 292.49–294.37, 302.62–304.49, and 304.14–306.01 GHz, with a spectral resolution of 977 kHz (0.963 km s^{-1}).

We used the Common Astronomy Software Application (CASA 5.4.1) for data reduction and imaging using the ALMA data reduction pipeline (McMullin et al. 2007). We used the Perley-Butler 2017 flux calibrator model for flux calibration using the task SETJY (Perley & Butler 2017). After the initial data reduction using the CASA pipeline, we utilized task MSTRANSFORM to separate the target data G358.93–0.03 with all the available rest frequencies. The continuum image is created by selecting line-free channels. Before creating the spectral images, the continuum emission is subtracted from the spectral data using the UVCONTSUB task. To create the spectral images of G358.93–0.03, we used Briggs weighting (Briggs 1995) and a robust value of 0.5. We used the CASA task IMPBCOR to correct the synthesized beam pattern in continuum and spectral images.

3 RESULTS

3.1 Continuum emission

3.1.1 Submillimetre wavelength continuum emission towards G358.93–0.03

The continuum emission of G358.93–0.03 is observed at 303.39 GHz (988 μm), as shown in Fig. 1. The synthesized beam size is 0.412 arcsec $\times$ 0.363 arcsec. In the continuum emission image, we observe eight submillimetre continuum sources, G358.93–0.03 MM1 to G358.93–0.03 MM8. Among the eight sources, G358.93–0.03 MM1 and G358.93–0.03 MM3 are known as hot molecular cores (Brogan et al. 2019). Additionally, we also detected two other continuum sources associated with G358.93–0.03 MM1 and G358.93–0.03 MM2. We define these two continuum sources as G358.93–0.03 MM1A and G358.93–0.03 MM2A. We individually fit the 2D Gaussian for each source in G358.93–0.03 using the CASA task IMFIT and estimate the integrated flux density, peak flux density, deconvolved source size, and RMS, which are shown in Table 1. Except for G358.93–0.03 MM2A and G358.93–0.03 MM8, we see that the continuum emissions of other sources are resolved. Brogan et al. (2019) also detected the submillimetre wavelength continuum emission from the eight individual continuum sources (G358.93–0.03 MM1 to G358.93–0.03 MM8) of G358.93–0.03 at frequencies of 195.58, 233.75, and 337.26 GHz.

3.1.2 Estimation of molecular hydrogen (H$_2$) column density and optical depth (τ) towards G358.93–0.03

Here, we focus on estimating the molecular hydrogen column densities from all continuum sources in G358.93–0.03. The peak flux density (S_ν) of the optically thin dust continuum emission can be expressed as

$$S_\nu = B_\nu(T_d)\tau_\nu\Omega_{\text{beam}}, \tag{1}$$

where the Planck function at dust temperature (T_d) is represented by $B_\nu(T_d$; Whittet 1992), τ_ν is the optical depth, and $\Omega_{\text{beam}} = (\pi/4\ln 2) \times \theta_{\text{major}} \times \theta_{\text{minor}}$ is the solid angle of the synthesized beam. The expression for the optical depth in terms of the mass density of dust can be written as,

$$\tau_\nu = \rho_d\kappa_\nu L, \tag{2}$$

where ρ_d is the mass density of the dust, κ_ν is the mass absorption coefficient, and L the path length. The mass density of the dust can be expressed in terms of the dust-to-gas mass ratio (Z),

$$\rho_d = Z\mu_H\rho_{H_2} = Z\mu_H N_{H_2}2m_H/L, \tag{3}$$

where μ_H is the mean atomic mass per hydrogen, ρ_{H_2} is the hydrogen mass density, m_H indicates the mass of hydrogen, and N_{H_2} is the column density of hydrogen. For the dust temperature, T_d, we adopt 150 K, as derived by Chen et al. (2020) for the two hot cores, G358.93–0.03 MM1 and G358.93–0.03 MM3. For the rest of the cores, we adopt a dust temperature of 30.1 K as estimated by Stecklum et al. (2021). We also take μ_H = 1.41 and Z = 0.01 (Cox & Pilachowski 2000). The peak flux density of all the continuum sources in G358.93–0.03 at frequency 303.39 GHz is listed in Table 1. From equations 1, 2, and 3, the column density of molecular hydrogen can be expressed as,

$$N_{H_2} = \frac{S_\nu/\Omega}{2\kappa_\nu B_\nu(T_d)Z\mu_H m_H}. \tag{4}$$
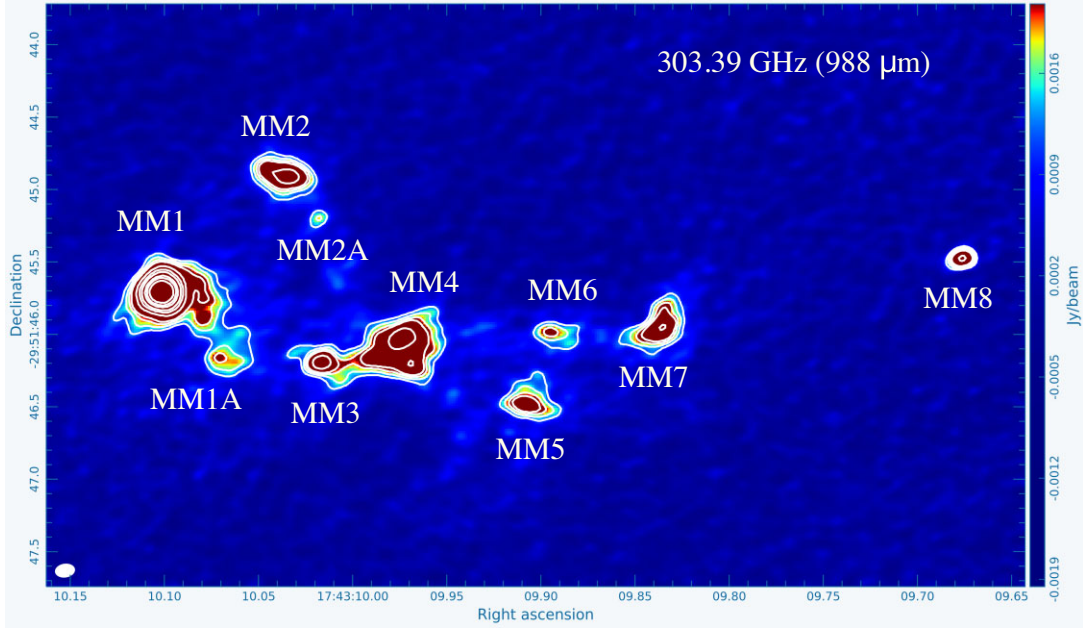
Figure 1. Continuum emission image of high-mass star-formation region G358.93–0.03 at a wavelength of 988 μm. The synthesized beam size (white circle) of the continuum image is 0.412 arcsec × 0.363 arcsec. The submillimetre continuum sources MM1–MM8 are located in the massive star-formation region G358.93–0.03. The contour (white colour) levels start at 3σ where σ is the RMS of the continuum emission image and the contour levels increase by a factor of $\sqrt{2}$.

Table 1. Summary of the continuum properties towards G358.93–0.03 at wavelength 988 μm.

Source	RA	Dec.	Deconvolved source size (arcsec × arcsec)	Integrated flux (mJy)	Peak flux (mJy beam^{-1})	RMS (μJy)	Remark
G358.93–0.03 MM1	17:43:10.1015	−29:51:45.7057	0.116 × 0.085	72.80 ± 2.20	34.81 ± 0.75	68.5	Resolved
G358.93–0.03 MM1A	17:43:10.0671	−29:51:46.4511	0.469 × 0.411	67.71 ± 2.60	3.53 ± 0.13	21.1	Resolved
G358.93–0.03 MM2	17:43:10.0357	−29:51:44.9019	0.231 × 0.088	14.20 ± 1.40	4.47 ± 0.35	35.5	Resolved
G358.93–0.03 MM2A	17:43:10.0209	−29:51:45.1577	−	2.30 ± 0.58	1.52 ± 0.18	20.3	Not resolved
G358.93–0.03 MM3	17:43:10.0145	−29:51:46.1933	0.072 × 0.019	6.12 ± 0.32	5.10 ± 0.16	18.6	Resolved
G358.93–0.03 MM4	17:43:09.9738	−29:51:46.0707	0.160 × 0.087	10.50 ± 2.42	4.38 ± 0.32	49.8	Resolved
G358.93–0.03 MM5	17:43:09.9063	−29.51:46.4814	0.245 × 0.078	7.80 ± 1.10	2.50 ± 0.48	30.4	Resolved
G358.93–0.03 MM6	17:43:09.8962	−29:51:45.9802	0.107 × 0.062	3.28 ± 0.21	1.98 ± 0.08	7.9	Resolved
G358.93–0.03 MM7	17:43:09.8365	−29:51:45.9498	0.216 × 0.116	13.91 ± 1.82	3.85 ± 0.39	38.5	Resolved
G358.93–0.03 MM8	17:43:09.6761	−29:51:45.4688	−	6.50 ± 0.11	4.582 ± 0.06	6.4	Not resolved

For the estimation of the mass absorption coefficient (κ_ν), we use the formula $\kappa_\nu = 0.90(\nu/230 \text{ GHz})^\beta$ cm^2 g^{-1} (Motogi et al. 2019), where $k_{230} = 0.90$ cm^2 g^{-1} indicates the emissivity of the dust grains at a gas density of 10^6 cm^{-3}. We use the dust spectral index $\beta \sim 1.7$ (Brogan et al. 2019). From equation 4, we find the column densities of molecular hydrogen (N_{H_2}) towards all observed continuum sources in G358.93–0.03, which we report in Table 2.

We also determine the value of the dust optical depth (τ_ν) using the following equation,

$$T_{mb} = T_d(1 - exp(-\tau_\nu)),\qquad(5)$$

where T_{mb} represents the brightness temperature and T_d is the dust temperature. For an estimation of the brightness temperature (T_{mb}), we use the Rayleigh–Jeans approximation, 1 Jy beam$^{-1} \equiv 118$ K. Using equation 5, we estimate the dust optical depth towards all observed continuum sources in G358.93–0.03 (listed in Table 2). We find that the optical depth of all observed continuum sources is less than 1, indicating that all observed continuum sources in G358.93–0.03 are optically thin at the frequency of 303.39 GHz.

Table 2. Column densities of molecular H_2 and optical depths towards the continuum sources in G358.93–0.03.

Source	N_{H_2} (cm^{-2})	T_{mb} (K)	τ
G358.93–0.03 MM1	$(3.10 \pm 0.2) \times 10^{24}$	4.10	27.72×10^{-3}
G358.93–0.03 MM1A	$(1.21 \pm 0.8) \times 10^{24}$	0.41	13.71×10^{-3}
G358.93–0.03 MM2	$(1.53 \pm 0.7) \times 10^{24}$	0.52	17.66×10^{-3}
G358.93–0.03 MM2A	$(5.22 \pm 0.2) \times 10^{23}$	0.17	5.93×10^{-3}
G358.93–0.03 MM3	$(3.51 \pm 0.7) \times 10^{23}$	0.60	4.01×10^{-3}
G358.93–0.03 MM4	$(1.50 \pm 0.3) \times 10^{24}$	0.51	17.29×10^{-3}
G358.93–0.03 MM5	$(8.59 \pm 0.5) \times 10^{23}$	0.29	9.84×10^{-3}
G358.93–0.03 MM6	$(6.80 \pm 0.6) \times 10^{23}$	0.23	7.70×10^{-3}
G358.93–0.03 MM7	$(1.32 \pm 0.5) \times 10^{24}$	0.45	15.06×10^{-3}
G358.93–0.03 MM8	$(1.57 \pm 0.8) \times 10^{24}$	0.54	18.13×10^{-3}

3.2 Line emission from G358.93–0.03

From the spectral images of G358.93–0.03, we see that only the spectra of G358.93–0.03 MM1 and G358.93–0.03 MM3 show any
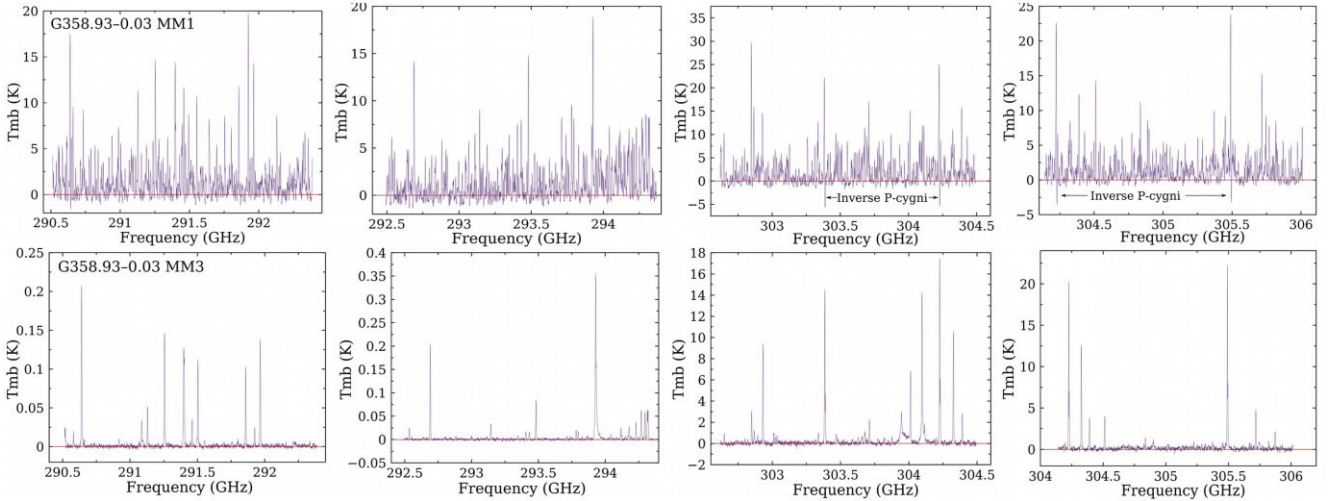
Figure 2. Sub-millimetre wavelength molecular emission spectra towards G358.93–0.03 MM1 (upper panel) and G358.93–0.03 MM3 (lower panel), from ALMA band 7. The spectral resolution of the molecular spectra is 976.56 kHz. The red horizontal lines indicate the baseline of the molecular spectra.

line emission. The synthesized beam sizes of the spectral images of G358.93–0.03 at frequency ranges of 290.51–292.39, 292.49–294.37, 302.62–304.49, and 304.14–306.01 GHz are 0.425 arcsec × 0.369 arcsec, 0.427 arcsec × 0.376 arcsec, 0.413 arcsec × 0.364 arcsec, and 0.410 arcsec × 0.358 arcsec, respectively. We extract the molecular spectra from G358.93–0.03 MM1 and G358.93–0.03 MM3 by drawing a 0.912 arcsec diameter circular region, which is larger than the line emitting regions of G358.93–0.03 MM1 and G358.93–0.03 MM3. The phase centre of G358.93–0.03 MM1 is RA (J2000) = $17^h43^m10^s.101$, Dec. (J2000) = –$29°51'45''.693$. The phase centre of G358.93–0.03 MM3 is RA (J2000) = $17^h43^m10^s.0144$, Dec. (J2000) = –$29°51'46''.193$. The resultant spectra of G358.93–0.03 MM1 and G358.93–0.03 MM3 are shown in Fig. 2. From the spectra, it can be seen that G358.93–0.03 MM1 is more chemically rich than G358.93–0.03 MM3. Additionally, we also observe the signature of an inverse P Cygni profile associated with the CH_3OH emission lines towards G358.93–0.03 MM1. This may indicate that the hot molecular core G358.93–0.03 MM1 is undergoing infall. We do not observe any evidence of an inverse P Cygni profile in the spectra of G358.93–0.03 MM3. The systematic velocities (V_{LSR}) of G358.93–0.03 MM1 and G358.93–0.03 MM3 are –16.5 and –18.2 km s^{-1}, respectively, (Brogan et al. 2019).

3.2.1 *Identification of CH_2OHCHO towards G358.93–0.03 MM1*

To identify the rotational emission lines of CH_2OHCHO, we assume local thermodynamic equilibrium (LTE) and use the Cologne Data base for Molecular Spectroscopy (CDMS; Müller et al. 2005). For LTE modelling, we use CASSIS (Vastel et al. 2015). The LTE assumption is valid in the inner region of G358.93–0.03 MM1 because the gas density of the warm inner region of the hot core is 2×10^7 cm^{-3} (Stecklum et al. 2021). To fit the LTE model spectra of CH_2OHCHO over the observed molecular spectra, we use the Markov chain Monte Carlo (MCMC) algorithm in CASSIS. Previously, Gorai et al. (2020) discussed the fitting of the LTE model spectrum using MCMC in detail. We have identified a total of 75 transitions of CH_2OHCHO towards G358.93–0.03 MM1 between the frequency ranges of 290.51–292.39, 292.49–294.37, 302.62–304.49,

and 304.14–306.01 GHz. The upper-level energies of the identified 75 transitions of CH_2OHCHO vary from 63.86 to 1362.19 K. Among the detected 75 transitions, we find that only 14 transitions of CH_2OHCHO are not blended, and these lines are identified to be higher than 4σ (confirmed from LTE modelling). The upper-level energies of the non-blended transitions of CH_2OHCHO vary between 69.40 and 670.33 K. There are no missing transitions in CH_2OHCHO in the observed frequency ranges. The blended transitions of CH_2OHCHO will not be considered in our modelling. From the LTE modelling, the best-fitting column density of CH_2OHCHO is found to be $(1.52 \pm 0.9) \times 10^{16}$ cm^{-2} with an excitation temperature of 300 ± 68.5 K and a source size of 0.45 arcsec. The full width at half-maximum (FWHM) of the LTE spectra of CH_2OHCHO is 3.35 km s^{-1}. We observed that the FWHM of the spectra of CH_2OHCHO is nearly similar to the FWHM of another molecule CH_3CN towards G358.93–0.03 MM1, which was estimated by Brogan et al. (2019). The LTE-fitted rotational emission spectra of CH_2OHCHO are shown in Fig. 3. In addition to CH_2OHCHO, the hot molecular core G358.93–0.03 MM1 also contains several other complex organic molecules, including CH_3OCHO, CH_3COOH, CH_3NH_2, CH_3OH, CH_3SH, C_2H_5CN, and C_2H_3CN, which we discuss in a separate paper.

We report the details of all the detected CH_2OHCHO lines in Table 3. Additionally, we also fitted the Gaussian model over the non-blended emission lines of CH_2OHCHO to estimate the proper FWHM in km s^{-1} and integrated intensity ($\int T_{mb}dV$) in K km s^{-1}. We have observed three different non-blended emission lines of CH_2OHCHO at frequencies of 291.784, 292.536, and 292.737 GHz that contain multiple transitions of CH_2OHCHO. These transitions are reported in Table 3. We cannot separate these observed transitions as they are very close to each other, i.e. blended with each other. To obtain the line parameters of those transitions of CH_2OHCHO, we have fitted a multiple-component Gaussian using the Levenberg–Marquardt algorithm in CASSIS to the observed spectra. For multiple Gaussian fittings, we have used fixed values of velocity separation and the expected line intensity ratio. During the fitting of a multicomponent Gaussian, only the FWHM is kept as a free parameter. This method works well in the observed spectral profiles around 291.784, 292.536, and 292.737 GHz of CH_2OHCHO. The summary of the
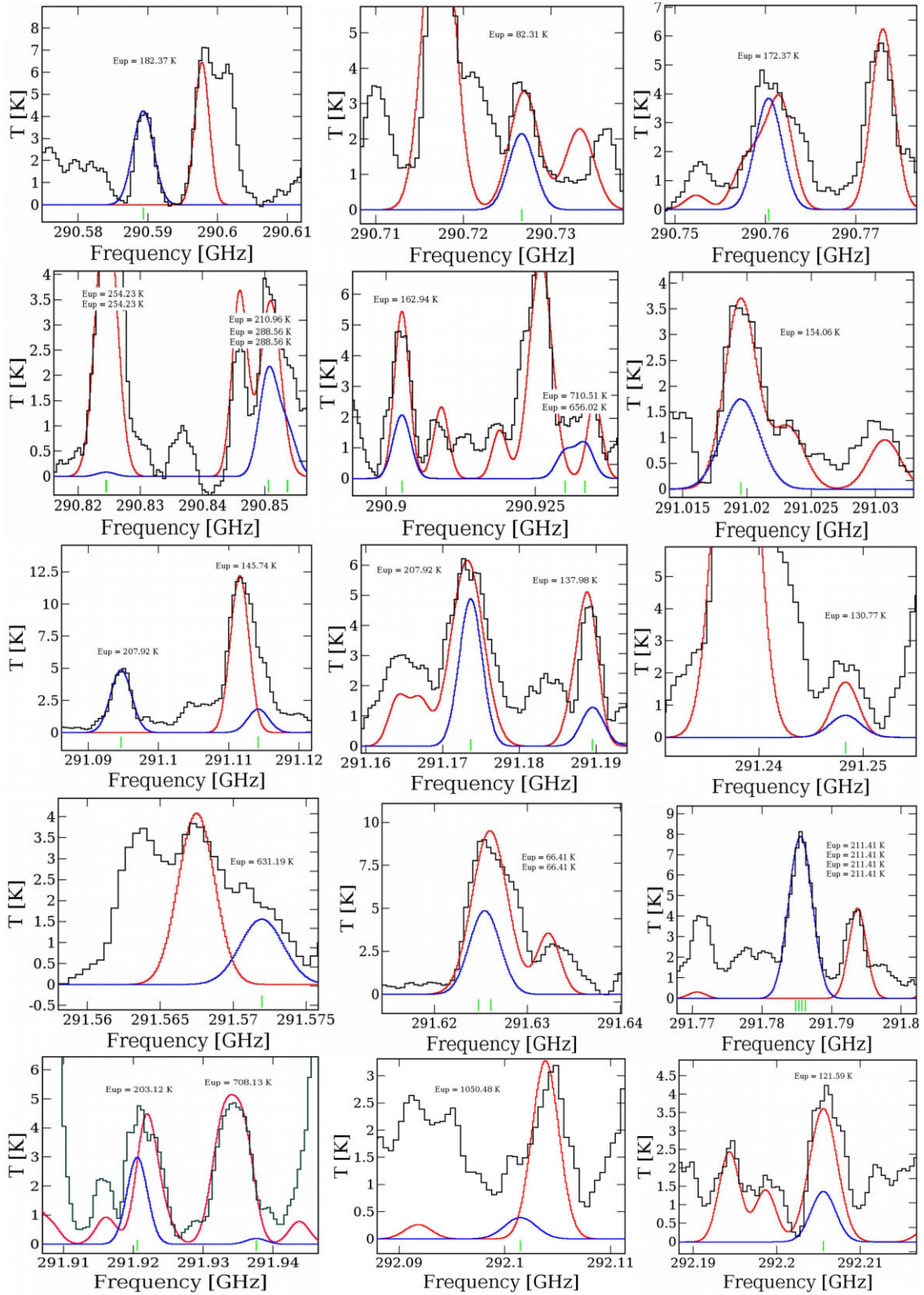
Figure 3. Rotational emission lines of CH$_2$OHCHO towards the hot molecular core G358.93–0.03 MM1. The black spectra are the observations spectra of G358.93–0.03 MM1. The blue spectra represent the LTE model spectrum of just CH$_2$OHCHO, while the red spectra are the LTE model spectra, including all species. The green vertical lines in the LTE spectra indicate the rest frequency positions of the detected transitions of CH$_2$OHCHO.
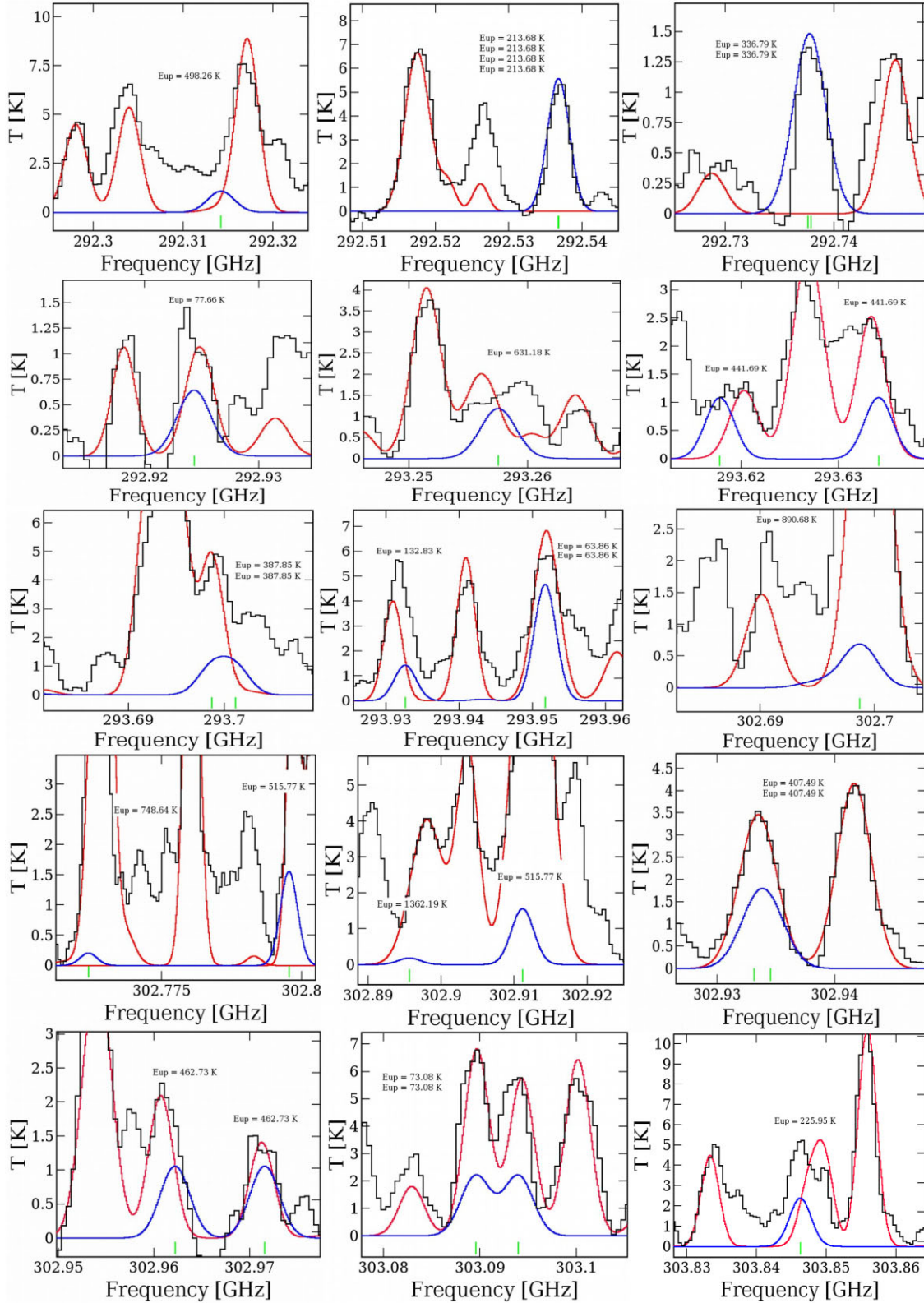
Figure 3. Continued.

detected transitions and spectral line properties of CH_2OHCHO is presented in Table 3.

To determine the fractional abundance of CH_2OHCHO, we use the column density of CH_2OHCHO inside the 0.45 arcsec beam,

and divide it by the H_2 column density found in Section 3.1.2. The fractional abundance of CH_2OHCHO with respect to H_2 towards the G358.93–0.03 MM1 is $(4.90 \pm 2.92) \times 10^{-9}$, where the column density of H_2 towards the G358.93–0.03 MM1 is $(3.10 \pm 0.2) \times$

Figure 3. Continued.

Table 3. Summary of the line parameters of CH$_2$OHCHO towards G358.93–0.03 MM1.

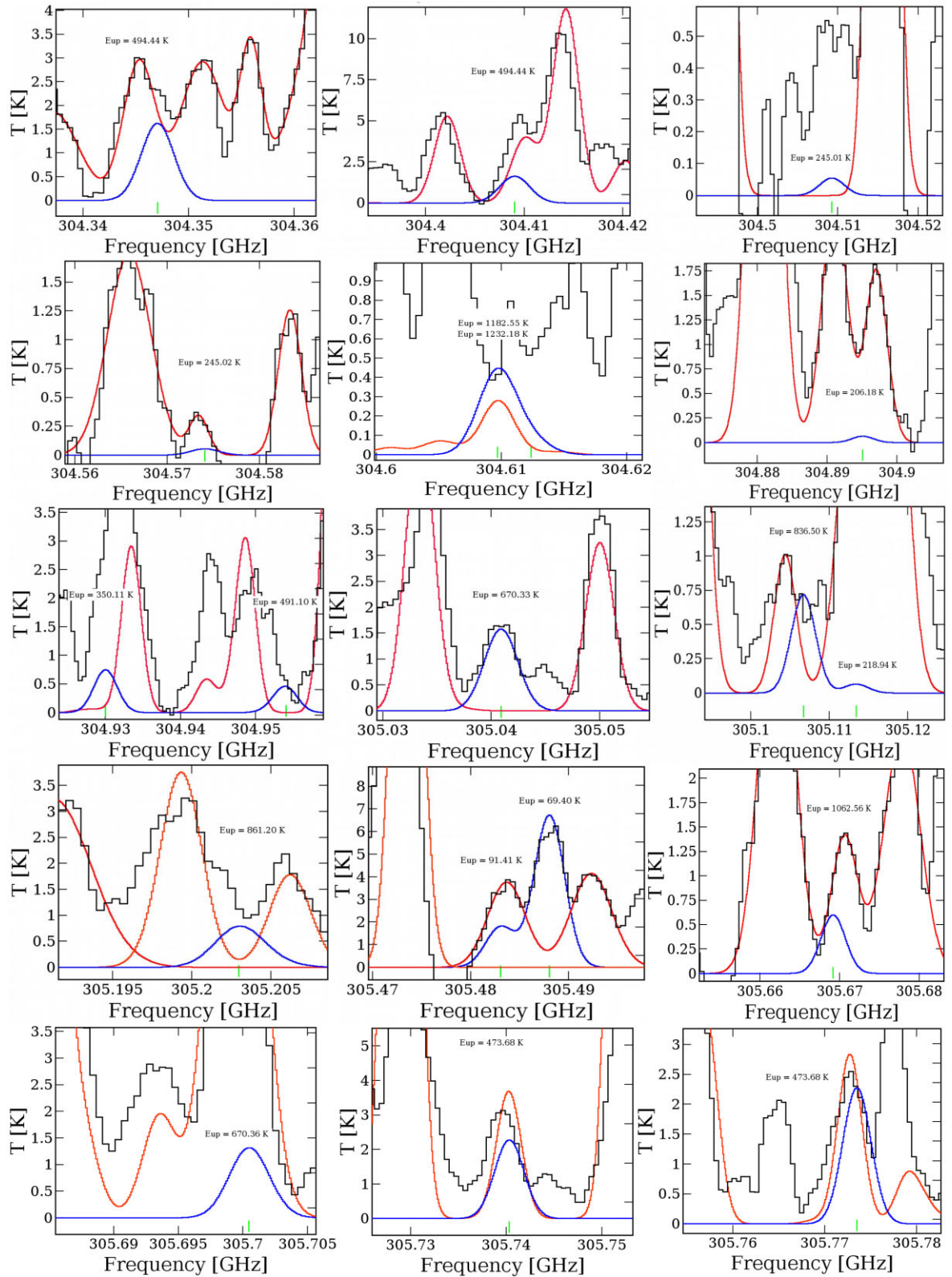| Observed frequency (GHz)	Transition ($J'_{K'_a K'_c}$–$J''_{K''_a K''_c}$)	E_u (K)	A_{ij} (s^{-1})	G_{up}	FWHM (km s^{-1})	Optical depth (τ)	I_p [†] (K)	$\int T_{mb}dV$ (K km s^{-1})	Remark
290.589*	18(12,6)–18(11,7)	182.3	2.59×10^{-4}	37	3.2 ± 0.2	1.2×10^{-2}	4.1	11.9 ± 1.2	Non-blended
290.726	15(5,10)–14(4,11)	82.3	2.23×10^{-4}	31	–	1.3×10^{-2}	3.6	–	Blended with DCOOH
290.760*	17(12,6)–17(11,7)	172.3	2.39×10^{-4}	35	–	1.0×10^{-2}	4.8	–	Blended with CH$_3$O^{13}CHO
290.824	25(11,15)–24(11,14)	254.2	7.78×10^{-6}	51	–	3.9×10^{-4}	5.7	–	Blended with CH$_3$OCHO
290.824	25(11,14)–24(11,13)	254.2	7.78×10^{-6}	51	–	3.9×10^{-4}	5.7	–	Blended with CH$_3$OCHO
290.850	26(4,22)–25(5,21)	210.9	3.16×10^{-4}	53	–	1.9×10^{-2}	3.7	–	Blended with CH$_3$COOH
290.853	33(1,32)–33(0,33)	288.5	6.82×10^{-5}	67	–	4.0×10^{-3}	2.5	–	Blended with H$_2$CCNH
290.853	33(2,32)–33(1,33)	288.5	6.82×10^{-5}	67	–	4.0×10^{-3}	2.5	–	Blended with H$_2$CCNH
290.902*	16(12,4)–16(11,5)	162.9	2.16×10^{-4}	33	–	9.7×10^{-3}	4.9	–	Blended with CH$_3$COOH
290.929	48(9,40)–48(8,41)	710.5	3.81×10^{-4}	97	–	8.0×10^{-3}	1.8	–	Blended with CH$_3$CH$_2$CN
290.933	44(13,32)–44(12,33)	656.0	4.49×10^{-4}	89	–	8.2×10^{-3}	2.8	–	Blended with CH$_3$CH$_2$CN
291.019*	15(12,4)–15(11,5)	154.0	1.89×10^{-4}	31	–	8.1×10^{-3}	3.5	–	Blended with CH$_3$COOH
291.094	27(2,25)–26(3,24)	207.9	5.47×10^{-4}	55	3.3 ± 0.3	3.4×10^{-2}	5.0	14.3 ± 2.3	Non-blended
291.114*	14(12,2)–14(11,3)	145.7	1.55×10^{-4}	29	–	6.5×10^{-3}	12.0	–	Blended with CH$_3$^{18}OH
291.173	27(3,25)–26(2,24)	207.9	5.47×10^{-4}	55	–	3.5×10^{-2}	5.7	–	Blended with CH$_3$CCH
291.189*	13(12,2)–13(11,3)	137.9	1.15×10^{-4}	27	–	4.5×10^{-3}	4.5	–	Blended with CH$_3$COCH$_3$
291.248*	12(12,0)–12(11,1)	130.7	6.40×10^{-5}	25	–	2.5×10^{-3}	2.3	–	Blended with HC^{18}ONH$_2$
291.571	43(13,30)–43(12,31)	631.1	4.47×10^{-4}	87	–	1.1×10^{-2}	2.4	–	Blended with ^{13}CH$_3$CH$_2$CN
291.624	11(7,5)–10(6,4)	66.4	4.49×10^{-4}	23	–	2.0×10^{-2}	8.9	–	Blended with DCONH$_2$
291.626	11(7,4)–10(6,5)	66.4	4.49×10^{-4}	23	–	2.0×10^{-2}	8.9	–	Blended with DCONH$_2$
291.784	28(1,27)–27(2,26)	211.4	6.46×10^{-4}	57	3.4 ± 0.1	4.2×10^{-2}	8.1	27.9 ± 4.8	Non-blended
291.784	28(2,27)–27(2,26)	211.4	9.58×10^{-6}	57	3.4 ± 0.1	4.2×10^{-2}	8.1	27.9 ± 4.8	Non-blended
291.784	28(1,27)–27(1,26)	211.4	9.58×10^{-6}	57	3.4 ± 0.1	4.2×10^{-2}	8.1	27.9 ± 4.8	Non-blended
291.786	28(2,27)–27(1,26)	211.4	6.46×10^{-4}	57	3.4 ± 0.1	4.2×10^{-2}	8.1	27.9 ± 4.9	Non-blended
291.920	26(4,23)–25(3,22)	203.1	4.41×10^{-4}	53	–	2.8×10^{-2}	4.7	–	Blended with ^{13}CH$_2$CHCN
291.937	47(11,37)–46(12,34)	708.1	8.68×10^{-5}	95	–	1.8×10^{-2}	4.8	–	Blended with CH$_3$COOH
292.101	58(11,47)–58(10,48)	1050.4	4.50×10^{-4}	117	–	3.7×10^{-3}	1.5	–	Blended with C$_2$H$_5$OH
292.205	19(5,15)–18(4,14)	121.5	2.13×10^{-4}	39	–	1.2×10^{-2}	4.2	–	Blended with E-CH$_3$CHO
292.314	41(5,36)–41(4,37)	498.2	2.79×10^{-4}	83	–	1.1×10^{-2}	7.5	–	Blended with CH$_3$OCHO
292.536	29(0,29)–28(1,28)	213.6	7.37×10^{-4}	59	3.3 ± 0.2	5.0×10^{-3}	5.3	15.4 ± 3.5	Non-blended
292.536	29(1,29)–28(1,28)	213.6	9.77×10^{-6}	59	3.3 ± 0.2	5.0×10^{-3}	5.3	15.4 ± 3.5	Non-blended
292.536	29(0,29)–28(0,28)	213.6	9.77×10^{-6}	59	3.3 ± 0.2	5.0×10^{-3}	5.3	15.4 ± 3.5	Non-blended
292.536	29(1,29)–28(0,28)	213.6	7.37×10^{-4}	59	3.3 ± 0.2	5.0×10^{-3}	5.3	15.4 ± 3.5	Non-blended
292.737	35(2,33)–35(1,34)	336.7	1.31×10^{-4}	71	3.2 ± 0.5	7.0×10^{-3}	1.3	3.5 ± 0.1	Non-blended
292.737	35(3,33)–35(2,34)	336.7	1.31×10^{-4}	71	3.2 ± 0.6	7.0×10^{-3}	1.3	3.5 ± 0.1	Non-blended
292.924	15(4,11)–14(3,12)	77.6	1.09×10^{-4}	31	–	6.1×10^{-3}	1.4	–	Blended with CH$_3$C$_3$N
293.257	43(13,31)–43(12,32)	631.1	4.54×10^{-4}	87	–	1.1×10^{-2}	1.5	–	Blended with HC$_3$N
293.617	39(4,35)–39(3,36)	441.7	2.37×10^{-4}	79	–	9.8×10^{-3}	1.0	–	Blended with ^{13}CH$_3$CH$_2$CN
293.634	39(5,35)–39(4,36)	441.7	2.37×10^{-4}	79	–	9.8×10^{-3}	2.5	–	Blended with CH$_3$OCH$_3$
293.698	37(3,34)–37(2,35)	387.8	1.88×10^{-4}	75	–	8.9×10^{-3}	5.0	–	Blended with CH$_3$COOH
293.701	37(4,34)–37(3,35)	387.8	1.88×10^{-4}	75	–	8.9×10^{-3}	5.0	–	Blended with CH$_3$COOH
293.932	20(5,16)–19(4,15)	132.8	2.21×10^{-4}	41	–	1.3×10^{-2}	5.6	–	Blended with CH$_2$CH^{13}CN
293.951	9(8,2)–8(7,3)	63.8	6.30×10^{-4}	19	–	2.2×10^{-2}	5.7	–	Blended with ^{13}CH$_3$CH$_2$CN
293.951	9(8,1)–8(7,2)	63.8	6.30×10^{-4}	19	–	2.2×10^{-2}	5.7	–	Blended with ^{13}CH$_3$CH$_2$CN
302.698	52(14,39)–52(13,40)	890.6	5.30×10^{-4}	105	–	6.1×10^{-3}	6.5	–	Blended with CH$_2$DOH
302.761	48(12,36)–47(13,35)	748.6	1.07×10^{-4}	97	–	1.8×10^{-3}	6.3	–	Blended with HC^{18}ONH$_2$
302.797	38(13,25)–38(12,36)	515.7	4.70×10^{-4}	77	–	1.3×10^{-2}	5.3	–	Blended with CH$_3$SH
302.895	66(13,53)–66(12,54)	1362.2	5.32×10^{-4}	133	–	1.6×10^{-3}	4.0	–	Blended with CH$_3$O^{13}CHO
302.911	38(13,26)–38(12,27)	515.7	4.71×10^{-4}	77	–	1.2×10^{-2}	15.3	–	Blended with CH$_3$OH
302.933	38(3,35)–38(2,36)	407.5	2.09×10^{-4}	77	–	8.5×10^{-3}	3.5	–	Blended with H^{13}CCCN
302.934	38(4,35)–38(3,36)	407.5	2.09×10^{-4}	77	–	8.5×10^{-3}	3.5	–	Blended with H^{13}CCCN
302.962	40(4,36)–40(3,37)	462.7	2.54×10^{-4}	81	–	9.5×10^{-3}	2.2	–	Blended with CH$_2$CH^{13}CN
302.971	40(5,36)–40(4,37)	462.7	2.54×10^{-4}	81	–	9.5×10^{-3}	1.5	–	Blended with HCOOD
303.089	12(7,6)–11(6,5)	73.0	4.68×10^{-4}	25	–	2.1×10^{-2}	7.2	–	Blended with NH$_2$CO$^+$
303.094	12(7,5)–11(6,6)	73.0	4.68×10^{-4}	25	–	2.0×10^{-2}	6.8	–	Blended with c-HCOOH
303.846	27(4,23)–26(5,22)	225.9	3.86×10^{-4}	55	–	2.1×10^{-2}	5.2	–	Blended with D^{13}CCCN
304.347	37(13,24)–37(12,25)	494.4	4.71×10^{-4}	75	–	1.4×10^{-2}	3.3	–	Blended with CH$_3$CDO
304.409	37(13,25)–37(12,26)	494.4	4.71×10^{-4}	75	–	1.4×10^{-2}	5.3	–	Blended with NCHCCO
304.509	26(9,18)–25(9,16)	245.0	9.75×10^{-6}	53	–	4.8×10^{-4}	0.5	–	Blended with ^{13}CH$_3$CN
304.574	26(9,17)–25(9,16)	245.0	9.76×10^{-6}	53	–	4.8×10^{-4}	0.3	–	Blended with C$_2$H$_5$C^{15}N
304.609	61(14,48)–61(13,49)	1182.5	5.58×10^{-4}	123	–	2.8×10^{-3}	0.8	–	Blended with C$_2$H$_5$CN
304.612	61(17,45)–60(18,42)	1232.1	1.07×10^{-4}	123	–	4.6×10^{-4}	0.8	–	Blended with C$_2$H$_5$CN
304.895	25(6,19)–24(6,18)	206.1	1.05×10^{-5}	51	–	5.7×10^{-4}	0.9	–	Blended with H^{13}CCN

Table 3 *– continued*

Observed frequency (GHz)	Transition ($J'_{K'_a K'_c} - J''_{K''_a K''_c}$)	E_u (K)	A_{ij} (s^{-1})	G_{up}	FWHM (km s^{-1})	Optical depth (τ)	I_p † (K)	$\int T_{mb} dV$ (K km s^{-1})	Remark
304.930	33(7,26)–32(8,25)	350.1	1.50×10^{-4}	67	–	6.6×10^{-3}	4.9	–	Blended with CH$_3$OCHO
304.954	39(9,30)–38(10,29)	491.1	1.17×10^{-4}	79	–	3.8×10^{-3}	1.8	–	Blended with HC(O)NH$_2$
305.040	47(7,40)–47(6,41)	670.0	3.90×10^{-4}	95	3.4 ± 0.6	6.1×10^{-3}	1.6	5.806 ± 1.87	Non-blended
305.106	52(10,43)–52(9,44)	836.5	4.59×10^{-4}	105	–	3.1×10^{-3}	0.7	–	Blended with CH$_3$COOH
305.113	26(6,21)–25(6,20)	218.9	1.05×10^{-5}	53	–	2.6×10^{-4}	3.0	–	Blended with C$_2$H$_5$CN
305.203	51(14,38)–51(13,39)	861.2	5.38×10^{-4}	103	–	3.1×10^{-3}	3.2	–	Blended with CH$_2$DCHO
305.483	16(5,11)–15(4,12)	91.4	2.29×10^{-4}	33	–	5.4×10^{-3}	3.9	–	Blended with CH$_3$COOH
305.488*	10(8,3)–9(7,2)	69.4	6.41×10^{-4}	21	3.4 ± 0.5	1.1×10^{-2}	6.2	24.2 ± 2.6	Non-blended
305.669	57(15,42)–57(14,43)	1062.5	5.56×10^{-4}	115	–	1.9×10^{-3}	1.4	–	Blended with CH$_3$COOH
305.700	47(8,40)–47(7,41)	670.3	3.93×10^{-4}	95	–	4.1×10^{-3}	15.6	–	Blended with CH$_2$DCHO
305.740	36(13,23)–36(12,24)	473.6	4.71×10^{-4}	73	–	7.0×10^{-3}	3.5	–	Blended with CH$_3$COOH
305.773	36(13,24)–36(12,25)	473.6	4.71×10^{-4}	73	–	7.0×10^{-3}	2.5	–	Blended with CH$_3^{18}$OH

Notes. * There are two transitions that have close frequencies (≤ 100 kHz), and only the frequency of the first transition is shown.
$^\dagger I_p$ is the peak intensity of the emission lines of CH$_2$OHCHO.

10^{24} cm^{-2}. Recently, Mininni et al. (2020) found that the abundance of CH$_2$OHCHO towards another hot molecular core, G31.41 + 0.31, was $(5.0 \pm 1.4) \times 10^{-9}$, which is close to our derived abundance of CH$_2$OHCHO towards G358.93–0.03 MM1. This indicates that the chemical formation route(s) of CH$_2$OHCHO towards the G358.93–0.03 MM1 may be similar to those in G31.41 + 0.31.

3.2.2 Searching for CH$_2$OHCHO towards G358.93–0.03 MM3

After the successful detection of CH$_2$OHCHO in G358.93–0.03 MM1, we also search for emission lines of CH$_2$OHCHO towards G358.93–0.03 MM3, which yield no detection. The derived upper-limit column density of CH$_2$OHCHO towards this core is $\leq (3.52 \pm 1.2) \times 10^{15}$ cm^{-2}. The upper limit of the fractional abundance is $\leq (1.01 \pm 0.40) \times 10^{-8}$.

3.3 Spatial distribution of CH$_2$OHCHO towards G358.93–0.03 MM1

We create the integrated emission maps (moment zero maps) of CH$_2$OHCHO towards G358.93–0.03 MM1 using the CASA task IMMOMENTS. In task IMMOMENTS, we use channels corresponding to the velocity ranges, where the emission lines of CH$_2$OHCHO were detected. The integrated emission maps are shown in Fig. 4. After the extraction, we apply the CASA task IMFIT to fit the 2D Gaussian over the integrated emission maps of CH$_2$OHCHO to estimate the size of the emitting regions. The following equation is used

$$\theta_S = \sqrt{\theta_{50}^2 - \theta_{beam}^2}, \qquad (6)$$

where θ_{beam} is the half-power width of the synthesized beam and $\theta_{50} = 2\sqrt{A/\pi}$ denotes the diameter of the circle whose area is surrounded by the 50 per cent line peak of CH$_2$OHCHO (Rivilla et al. 2017). The derived sizes of the emitting regions of CH$_2$OHCHO and velocity ranges at different frequencies are listed in Table 4. The synthesized beam sizes of the integrated emission maps at 290.589, 291.094, 291.784, 292.536, 292.737, 305.040, and 305.488 GHz are 0.425 arcsec × 0.369 arcsec, 0.426 arcsec × 0.368 arcsec, 0.427 arcsec × 0.376 arcsec, 0.428 arcsec × 0.377 arcsec, 0.413 arcsec × 0.364 arcsec, 0.415 arcsec × 0.368 arcsec, and 0.410 arcsec × 0.358 arcsec, respectively. We observe that the estimated emitting region of CH$_2$OHCHO is comparable to or slightly greater than the synthesized beam sizes of the integrated emission maps. This indicates that the

detected CH$_2$OHCHO transition lines are not spatially resolved or are only marginally resolved towards G358.93–0.03 MM1. Hence, we cannot draw any conclusions regarding the morphology of the spatial distributions of CH$_2$OHCHO. Higher spatial and angular resolution observations are required to understand the spatial distribution of CH$_2$OHCHO towards G358.93–0.03 MM1.

4 DISCUSSION

In this section, we compare the derived abundance of CH$_2$OHCHO in G358.93–0.03 MM1 with that of other hot cores and corinos. We also discuss the possible pathways for the formation of CH$_2$OHCHO in the context of hot molecular cores. Finally, we compare the observed abundance with those derived from chemical models.

4.1 Comparison with other sources

We list the abundances of CH$_2$OHCHO towards IRAS 16293–2422 B, NGC 7129 FIRS 2, NGC 1333 IRAS2A, Sgr B2 (N), G31.41+0.31, and G10.47+0.0 taken from the literature in Table 5. We note that for NGC 1333 IRAS 2A, Coutens et al. (2015) did not actually derive an abundance with respect to H$_2$ but instead with respect to (CH$_2$OH)$_2$ and CH$_3$OCHO. We, therefore, used their derived column density of CH$_2$OHCHO as well as the column density of H$_2$ as derived by Taquet et al. (2015) to infer an abundance with respect to H$_2$. Using the rotational diagram, Coutens et al. (2015) derived the column density of CH$_2$OHCHO towards NGC 1333 IRAS2A as 2.4×10^{15} cm^{-2} with a rotational temperature of 130 K. The column density of molecular hydrogen towards NGC 1333 IRAS2A is 5.0×10^{24} cm^{-2} (Taquet et al. 2015). To determine the fractional abundance of CH$_2$OHCHO with respect to H$_2$ towards NGC 1333 IRAS2A, we use the column density of CH$_2$OHCHO, which is divided by the column density of H$_2$. We deduce a fractional abundance for CH$_2$OHCHO towards NGC 1333 IRAS2A with respect to H$_2$ of 4.8×10^{-10}.

Our estimate for the abundance of CH$_2$OHCHO towards G358.93–0.03 MM1 [$(4.90 \pm 2.92) \times 10^{-9}$] is quite similar to that of the hot molecular core G31.41+0.31 and the hot corino object IRAS 16293–2422 B while approximately one order of magnitude higher than that of G10.47+0.03, Sgr B2 (N), NGC 1333 IRAS 2A, and NGC 7129 FIRS 2. The similarity among G358.93–0.03 MM1, G31.41 + 0.31, and IRAS 16293–2422 B may indicate that the formation route(s) of CH$_2$OHCHO may be similar in all three sources.
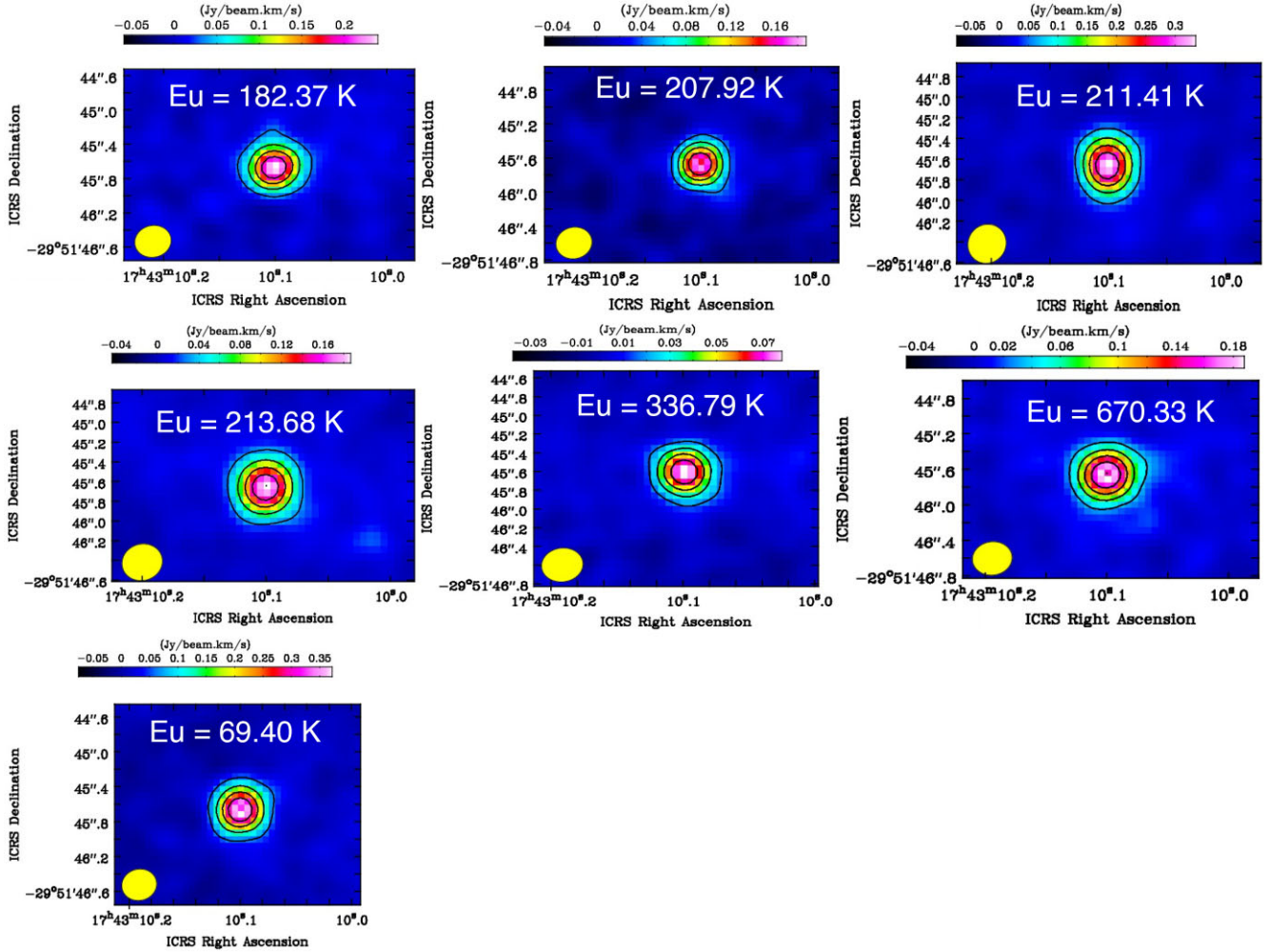
Figure 4. Integrated emission maps (moment zero) of CH₂OHCHO towards G358.93–0.03 MM1. The contour levels are at 20, 40, 60, and 80 per cent of the peak flux. Yellow circles represent the synthesized beams of the integrated emission maps.

Table 4. Estimated emitting regions of CH₂OHCHO towards the G358.93–0.03 MM1.

Observed frequency (GHz)	E_u (K)	Emitting region (arcsec)	Velocity ranges (km s⁻¹)
290.589*	182.37	0.410	−14.29 to −19.61
291.094	207.92	0.412	−13.39 to −18.68
291.784	211.41	0.413	−14.38 to −20.57
292.536	213.68	0.414	−13.35 to −19.31
292.737	336.79	0.415	−14.40 to −19.22
305.040	670.33	0.411	−13.34 to −18.44
305.488*	69.40	0.410	−14.14 to −18.79

Note. ∗There are two transitions that have close frequencies (≤100 kHz), and only the frequency of the first transition is shown.

4.2 Possible formation mechanisms of CH₂OHCHO towards hot molecular cores and hot corinos

To date, only a few efficient formation pathways of CH₂OHCHO have been proposed on grain-surfaces in hot molecular cores and hot corinos (Garrod & Herbst 2006; Garrod et al. 2008; Garrod 2013; Coutens et al. 2018; Rivilla et al. 2019; Mininni et al. 2020). In the high-temperature (≥100 K) regime, the radicals gain sufficient

Table 5. Abundance of CH₂OHCHO in different objects.

Source Names	X(CH₂OHCHO)	References
G358.93–0.03 MM1	$(4.90 \pm 2.92) \times 10^{-9}$	This paper
IRAS 16293–2422 B	5.8×10^{-9}	(Jørgensen et al. 2012)
NGC 7129 FIRS 2	5.0×10^{-10}	(Fuente et al. 2014)
NGC 1333 IRAS2A	4.8×10^{-10}	See Section 4.1
Sgr B2 (N)	1.6×10^{-10}	(Xue et al. 2019)
G31.41+0.31	$(5.0 \pm 1.4) \times 10^{-9}$	(Mininni et al. 2020)
G10.47+0.03	9.6×10^{-10}	(Mondal et al. 2021)

energy to diffuse across the surface and react to create complex organic molecules (Mininni et al. 2020). Initially, two main formation pathways were proposed for the formation of CH₂OHCHO:

$$HCO + CH_2OH \rightarrow CH_2OHCHO \qquad (1),$$

and

$$CH_3OH + HCO \rightarrow CH_2OHCHO + H \qquad (2).$$
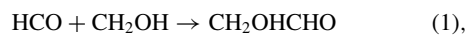
In reaction 1, radical HCO and radical CH₂OH react with each other on the grain-surfaces to form CH₂OHCHO (Garrod et al. 2008; Garrod 2013; Coutens et al. 2018; Rivilla et al. 2019). This

reaction appears to be responsible for the production of CH$_2$OHCHO towards IRAS 16293–2422 B and G31.41+0.31 (Jørgensen et al. 2012; Rivilla et al. 2019; Mininni et al. 2020). In reaction 2, the radicals HCO and CH$_3$OH react with each other on the grain-surfaces to produce CH$_2$OHCHO, but this reaction has not yet been tested in a laboratory (Mininni et al. 2020). Initially, Fedoseev et al. (2015) and Chuang et al. (2016) experimentally studied the possible formation pathways of CH$_2$OHCHO on dust grains at low temperatures ($\sim$10 K). The experimental results of Fedoseev et al. (2015) and Chuang et al. (2016) were later confirmed by Simons, Lamberts & Cuppen (2020) by using microscopic kinetic Monte Carlo simulations based on ice chemistry.

4.3 Chemical modelling of CH$_2$OHCHO in hot molecular cores

To understand the formation mechanisms and abundance of CH$_2$OHCHO in hot molecular cores, Coutens et al. (2018) computed a two-phase warm-up chemical model using the gas grain chemistry code UCLCHEM (Holdship et al. 2017). They assumed a free fall collapse of a cloud (Phase I), followed by a warm-up phase (Phase II). In the first phase (Phase I), the gas density increased from n_H = 300 to 10^7 cm^{-3}, and they assumed a constant dust temperature of 10 K. In the second phase (phase II), the gas density remained constant at 10^7 cm^{-3}, whereas the dust temperature increased with time from 10 to 300 K. This phase was known as the warm-up phase. In the chemical network used by Coutens et al. (2018), the recombination of the radicals HCO and CH$_2$OH (Reaction 1) dominates the production of CH$_2$OHCHO on the grains. Reaction 1 is the most likely pathway because Butscher et al. (2015) tested this reaction in the laboratory and confirmed that the reaction produced CH$_2$OHCHO. In the warm-up phase, Coutens et al. (2018) showed that the abundance of CH$_2$OHCHO varied from $\sim$10^{-9} to 10^{-8} (see fig. 3 in Coutens et al. 2018). Coutens et al. (2018) did not include Reaction 2 (recombination of the radical HCO and CH$_3$OH) as earlier work by Woods et al. (2012) showed that by including Reaction 2, the estimated model abundance of CH$_2$OHCHO was as high as $\sim$10^{-5} (Woods et al. 2012). This modelled abundance of CH$_2$OHCHO by Reaction 2 does not match any of the observed abundances in the sample of objects considered here.

4.4 Comparison between observed and chemically modelled abundance of CH$_2$OHCHO

In order to understand the formation pathways of CH$_2$OHCHO towards G358.93–0.03 MM1, we compare our estimated abundance with the modelled ones from Coutens et al. (2018). This comparison is physically reasonable because the dust temperature of this source is 150 K, which is a typical hot core temperature, and the number density (n_H) of this source is $\sim$2 $\times$ 10^7 cm^{-3} (Chen et al. 2020; Stecklum et al. 2021). Hence, the two-phase warm-up chemical model based on the time-scales in Coutens et al. (2018) is appropriate for explaining the chemical evolution of CH$_2$OHCHO towards G358.93–0.03 MM1. Coutens et al. (2018) showed that the abundances of CH$_2$OHCHO varies between $\sim$10^{-9} and 10^{-8}. We find that our estimated abundance towards G358.93–0.03 MM1 is (4.90 $\pm$ 2.92) $\times$ 10^{-9}, which is in good agreement with the theoretical results in Coutens et al. (2018). This comparison indicates that the simplest sugar-like molecule, CH$_2$OHCHO, may form on the grain-surface via the reaction between radical HCO and radical CH$_2$OH (Reaction 1) towards G358.93–0.03 MM1. Of course, the modelled abundance of CH$_2$OHCHO is also similar to the observed abundance of CH$_2$OHCHO towards the hot molecular core G31.41+0.31 and

the hot corino object IRAS 16293–2422 B, indicating that Reaction 1 may be the most likely pathway for the production of CH$_2$OHCHO towards these two objects too. Radical HCO and radical CH$_2$OH may be created in the ISM by the hydrogenation of CO (CO + H$\rightarrow$HCO$^\bullet$ + H$\rightarrow$H$_2$CO$\rightarrow^\bullet$CH$_2$OH; Hama & Watanabe 2013). After hydrogenation, radical CH$_2$OH is converted into CH$_3$OH ($^\bullet$CH$_2$OH + H$\rightarrow$CH$_3$OH; Hama & Watanabe 2013). Our conclusion agrees with the recent work of Mininni et al. (2020), who also found that reaction 1 is the most efficient pathway for the formation of CH$_2$OHCHO towards the hot core G31.41+0.31, as well as other hot molecular cores.

5 CONCLUSIONS

We present the first detection of CH$_2$OHCHO using ALMA in the hot molecular core G358.93–0.03 MM1. We identify a total of 75 transitions of CH$_2$OHCHO, where the upper-level energies vary between 63.86 and 1362.19 K. The derived abundance of CH$_3$OCHO is (4.90 $\pm$ 2.92) $\times$ 10^{-9}. We compare our estimated abundance with that of other hot molecular cores and hot corinos and note that the abundance of CH$_2$OHCHO towards G358.93–0.03 MM1 is quite similar to that found towards another hot molecular core, G31.41+0.31, and the hot corino, IRAS 16293–2422 B (Jørgensen et al. 2012; Mininni et al. 2020). We discuss the possible formation mechanisms of CH$_2$OHCHO in hot molecular cores. We compare our estimated abundance of CH$_2$OHCHO with the theoretical abundance from the chemical model presented in Coutens et al. (2018) and find that they are similar. We conclude that CH$_2$OHCHO is most likely formed via the reaction of radical HCO and radical CH$_2$OH on the grain-surfaces in G358.93–0.03 MM1 and other hot molecular cores.

The identification of abundant CH$_2$OHCHO in G358.93–0.03 MM1 suggests that grain-surface chemistry is also efficient for the formation of other complex organic molecules in this hot molecular core, including isomers of CH$_2$OHCHO, CH$_3$OCHO, and CH$_3$COOH. Indeed, the highly chemically rich spectra and detection of CH$_2$OHCHO towards G358.93–0.03 MM1 make this object another ideal hot core to search for and study other complex organic molecules in star-forming regions. A spectral line study combined with a radiative transfer as well as a two-phase warm-up chemical model is required to understand the prebiotic chemistry of G358.93–0.03 MM1, which will be carried out in our follow-up study.

DATA AVAILABILITY

The plots within this paper and other findings of this study are available from the corresponding author on reasonable request.

The data used in this paper are available in the ALMA Science Archive (https://almascience.nrao.edu/asax/), under project code 2019.1.00768.S.

REFERENCES

Bayandina O. S., et al., 2022, AJ, 163, 83
Belloche A., Müller H. S. P., Menten K. M., Schilke P., Comit C., 2013, A&A, 559, A47
Beltrán M. T., Codella C., Viti S., Neri R., Cesaroni R., 2009, ApJ, 690, L93
Briggs D. S., 1995, PhD thesis, New Mexico Tech
Brogan C. L., et al., 2019, ApJ, 881, L39
Butscher T., Duvernay F., Theule P., Danger G., Carissan Y., Hagebaum-Reignier D., Chiavassa T., 2015, MNRAS, 453, 1587
Calcutt H., Viti S., Codella C., Beltrán M. T., Fontani F., Woods P. M., 2014, MNRAS, 443, 3157
Chen X., et al., 2020, Nat. Astron., 4, 1170
Chuang K. J., Fedoseev G., Ioppolo S., van Dishoeck E. F., Linnartz H., 2016, MNRAS, 455, 1702
Coutens A., Persson M. V., Jørgensen J. K., Wampfler S. F., Lykke J. M., 2015, A&A, 576, A5
Coutens A., Viti S., Rawlings J. M. C., Beltrán M. T., Holdship J., Jiménez-Serra I., Quénard D., Rivilla V. M., 2018, MNRAS, 475, 2
Cox A. N., Pilachowski C. A., 2000, Phys. Today, 53, 77
Fedoseev G., Cuppen H. M., Ioppolo S., Lamberts T., Linnartz H., 2015, MNRAS, 448, 1288
Fuente A., et al., 2014, A&A, 568, A65
Garrod R. T., 2013, ApJ, 765, 60
Garrod R. T., Herbst E., 2006, A&A, 457, 927
Garrod R. T., Widicus Weaver S. L., Herbst E., 2008, ApJ, 682, 283
Gorai P., Bhat B., Sil M., Mondal S. K. Ghosh R., Chakrabarti S. K., Das A., 2020, ApJ, 895, 86
Halfen D. T., Apponi A. J., Woolf N., Polt R., Ziurys L. M., 2006, ApJ, 639, 237
Hama T., Watanabe N., 2013, Chem. Rev., 113, 8783
Herbst E., van Dishoeck E. F., 2009, ARA&A, 47, 427
Holdship J., Viti S., Jiménez-Serra I., Makrymallis A., Priestley F., 2017, AJ, 154, 38
Hollis J. M., Lovas F. J., Jewell P. R., 2000, ApJ, 540, L107
Hollis J. M., Jewell P. R., Lovas F. J., Remijan A., 2004, ApJ, 613, L45
Hollis J. M., Vogel S. N., Snyder L. E., Jewell P. R., Lovas F. J., 2001, ApJ, 554, L81
Jørgensen J. K., Favre C., Bisschop S. E., Bourke T. L., van Dishoeck E. F., Schmalzl M., 2012, ApJ, 757, L4

Manna A., Pal S., 2023, Astrophys. Space Sci., 368, 33 https://doi.org/10.1007/s10509-023-04192-4
McMullin J. P., Waters B., Schiebel D., Young W., Golap K., 2007, in Shaw R. A., Hill F., Bell D. J., eds, Astronomical Society of the Pacific Conference Series, Vol. 376, Astronomical Data Analysis Software and Systems XVI, p. 127
Mininni C. et al., 2020, A&A, 644, A84
Mondal S. K. et al., 2021, ApJ, 922, 194
Motogi K., Hirota T., Machida M. N., Yonekura Y., MarekiH., Shigehisa T., Satoki M., 2019, ApJ, 877, L25
Müller H. S. P., Schlmöder F., Stutzki J., Winnewisser G., 2005, J. Mol. Struct., 742, 215
Nomura H., Millar T. J., 2004, A&A, 414, 409
Perley R. A., Butler B. J., 2017, ApJ, 230, 1538
Reid M. J., et al., 2014, ApJ, 783, 130
Rivilla V. M., Beltrán M. T., Cesaroni R., Fontani F., Codella C., ZhangQ., 2017, A&A, 598, A59
Rivilla V. M., Beltrán M. T., Vasyunin A., Caselli P., VitiS., Fontani F., Cesaroni R., 2019, MNRAS, 483, 806
Shimonishi T., Izumi N., Furuya K., Yasui C., 2021, ApJ, 2, 206
Simons M. A. J., Lamberts T., Cuppen H. M., 2020, A&A, 634, A52
Stecklum B., et al., 2021, A&A, 646, A161
Taquet V., López-Sepulcre A., Ceccarelli C., Neri R., Kahane C., CharnleyS., 2015, ApJ, 804, 81
Taquet V., Wirström E. S., Charnley S. B., 2016, ApJ, 821, 46
van Dishoeck E. F., Blake G. A., 1998, ARA&A, 36, 317
Vastel C., Bottinelli S., Caux E., Glorian J. -M., Boiziot M., 2015, CASSIS: A Tool to Visualize and Analyse Instrumental and Synthetic Spectra. Proceedings of the Annual meeting of the French Society of Astronomy and Astrophysics. France. p. 313
Viti S., Collings M. P., Dever J. W., McCoustra M. R. S., Williams D. A., 2004, MNRAS, 354, 1141
Whittet D. C. B., 1992, J. Brit. Astron. Assoc., 102, 230
Williams D. A., Viti S., 2014, Observational Molecular Astronomy: Exploring the Universe Using Molecular Line Emissions. Cambridge Univ. Press, Cambridge
Woods P. M., Kelly G., Viti S., Slater B., BrownW., Puletti F., Burke D. J., Raza Z., 2012, APJ, 750, 19
Xue C., Remijan A. J., Burkhardt A. M., Herbst E., 2019, ApJ, 871, 112

This paper has been typeset from a TEX/LATEX file prepared by the author.